PHYSICAL REVIEW B **104**, 224409 (2021)

Quantum magnetism of ferromagnetic spin dimers in α-KVOPO$_4$

Prashanta K. Mukharjee,[1,*] K. Somesh,[1,*] K. M. Ranjith,[2] M. Baenitz,[2] Y. Skourski,[3] D. T. Adroja,[4,5]
D. Khalyavin,[4] A. A. Tsirlin,[6,†] and R. Nath[1,‡]
[1]*School of Physics, Indian Institute of Science Education and Research, Thiruvananthapuram-695551, India*
[2]*Max Planck Institute for Chemical Physics of Solids, Nöthnitzer Strasse 40, 01187 Dresden, Germany*
[3]*Dresden High Magnetic Field Laboratory (HLD-EMFL), Helmholtz-Zentrum Dresden-Rossendorf, 01314 Dresden, Germany*
[4]*ISIS facility, Rutherford Appleton Laboratory, Chilton Oxon OX11 0QX, United Kingdom*
[5]*Highly Correlated Matter Research Group, Physics Department, University of Johannesburg, Auckland Park 2006, South Africa*
[6]*Experimental Physics VI, Center for Electronic Correlations and Magnetism, Institute of Physics,
University of Augsburg, 86135 Augsburg, Germany*

(Received 14 September 2021; revised 22 October 2021; accepted 24 November 2021; published 7 December 2021)

Magnetism of the spin-$\frac{1}{2}$ α-KVOPO$_4$ is studied by thermodynamic measurements, ^{31}P nuclear magnetic resonance, neutron diffraction, and density-functional band-structure calculations. Ferromagnetic Curie-Weiss temperature of $\theta_{\rm CW} \simeq 15.9$ K and the saturation field of $\mu_0 H_s \simeq 11.3$ T suggest the predominant ferromagnetic coupling augmented by a weaker antiferromagnetic exchange that leads to a short-range order below 5 K and the long-range antiferromagnetic order below $T_{\rm N} \simeq 2.7$ K in zero field. Magnetic structure with the propagation vector $\mathbf{k} = (0, \frac{1}{2}, 0)$ and the ordered magnetic moment of 0.58 μ_B at 1.5 K exposes a nontrivial spin lattice where strong ferromagnetic dimers are coupled antiferromagnetically. The reduction in the ordered magnetic moment with respect to the classical value (1 $\mu_{\rm B}$) indicates sizable quantum fluctuations in this setting, despite the predominance of ferromagnetic exchange. We interpret this tendency toward ferromagnetism as arising from the effective orbital order in the folded chains of the VO$_6$ octahedra.

DOI: 10.1103/PhysRevB.104.224409

I. INTRODUCTION

Anderson's superexchange theory [1] requires that interactions in 3*d* magnetic insulators are predominantly antiferromagnetic (AFM) in nature. Ferromagnetic (FM) interactions are only possible when magnetic ions are close apart and, for example, form 90° pathways in the vein of Goodenough-Kanamori rules [1], but in this case equally strong AFM interactions will typically occur between more distant atoms, unless special conditions such as charge order [2,3] or orbital order [4,5] are met. In contrast to dozens of well-documented material candidates for quantum AFM spin-$\frac{1}{2}$ chains, only a handful of FM spin-chain compounds have been reported [6,7]. This disparity is, in fact, not undesirable because spin-$\frac{1}{2}$ antiferromagnets show much stronger quantum fluctuations [8,9] than in the ferromagnetic case.

Here, we introduce a material that remarkably departs from this general paradigm. Featuring V^{4+} as the magnetic ion, α-KVOPO$_4$ is dominated by short-range FM interactions. It further reveals an antiferromagnetically ordered ground state caused by residual AFM long-range interactions, wherein more than 30% reduction in the respective ordered magnetic moment signals strong quantum fluctuations that are not expected in weakly coupled FM units, such as spin-$\frac{1}{2}$ FM chains in Li$_2$CuO$_2$ where the ordered moment is 1.0 μ_B within the experimental uncertainty [10].

α-KVOPO$_4$ belongs to the group of vanadyl compounds with the general formulas *A*VO*X*O$_4$ and *A*V*X*O$_4$F, where X = P or As, and *A* is a monovalent cation. The common crystallographic feature of this family is the presence of structural chains of the VO$_6$ octahedra linked by corner-sharing. The tetrahedral *X*O$_4$ groups connect the chains into a three-dimensional network, yet leaving large channels for the A^+ ions that remain sufficiently mobile, especially at elevated temperatures. This feature triggered interest in *A*VO*X*O$_4$ as potential battery materials [11–13], whereas concurrent magnetism studies have also led to very encouraging results.

From the magnetism perspective, the crucial feature of *A*VO*X*O$_4$ is that their structural chains are not the direction of predominant magnetic interactions, even though the intrachain V–V distances are much shorter than the interchain ones [14,15]. It has been shown that monoclinic NaVO*X*O$_4$ [16,17] and AgVOAsO$_4$ [14,18], as well as triclinic ε-LiVOPO$_4$ [19], all adopt an intriguing pattern of crossed bond-alternating spin chains, which are perpendicular to the structural chains. These compounds reveal a field-induced quantum phase transition and an unusual double-dome regime of Bose-Einstein condensation (BEC) of magnons in high magnetic fields [15].

In the following, we report a comprehensive study of α-KVOPO$_4$ [20,21], which was so far not on the radar of magnetism studies. It is compositionally similar but structurally different (structure: orthorhombic, space group: *Pna*2$_1$) from the *A*VO*X*O$_4$ compounds with *A* = Li, Na, and Ag. The

---

[*] These authors contributed equally to this work.
[†] altsirlin@gmail.com
[‡] rnath@iisertvm.ac.in

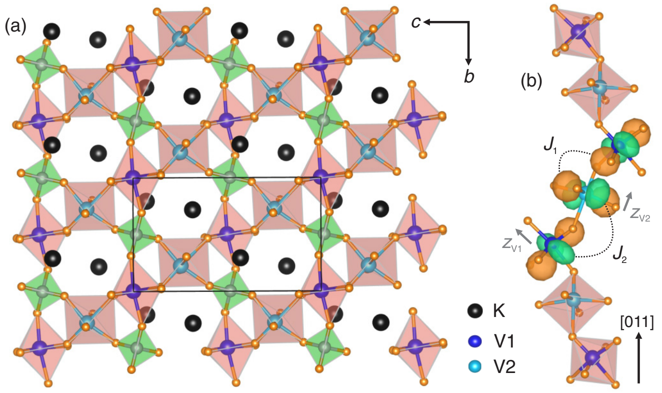

FIG. 1. (a) Crystal structure of α-KVOPO$_4$ features chains of VO$_6$ octahedra arranged along the [011] direction. (b) Each chain is folded and shows a nearly orthogonal configuration of the magnetic V d_{xy} orbitals because of the different directions of the local z-axes (short V–O bonds), which are denoted with the gray arrows. VESTA software [22] was used for crystal structure visualization.

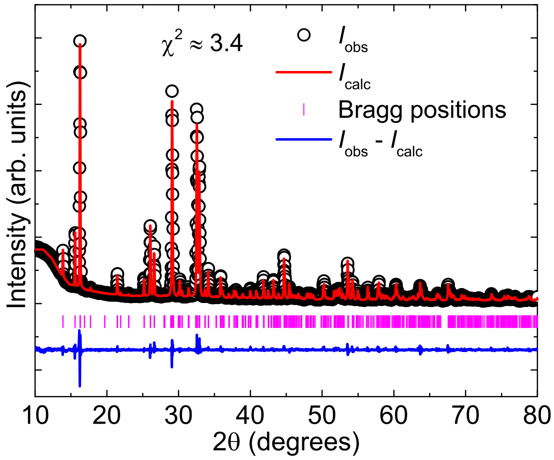

FIG. 2. Powder x-ray diffraction of α-KVOPO$_4$ collected at $T = 300$ K. The solid red line denotes the Rietveld refinement fit of the data. The Bragg peak positions are indicated by pink vertical bars and bottom blue line indicates the difference between experimental and calculated intensities.

larger K$^+$ ion stabilizes the noncentrosymmetric KTiOPO$_4$-type variety of the crystal structure, where chains of the VO$_6$ octahedra are folded and comprise two nonequivalent vanadium sites, V1 and V2 (Fig. 1). This structural modification has drastic repercussions for the magnetism. Whereas other compounds of the family are AFM in nature, α-KVOPO$_4$ is dominated by a FM interaction, yet it shows prominent quantum effects revealed by the reduced ordered magnetic moment.

II. METHODS

Polycrystalline sample of α-KVOPO$_4$ was synthesized by a solid-state reaction from the stoichiometric mixture of KPO$_3$ and V$_2$O$_4$ (Aldrich, 99.995%). The KPO$_3$ precursor was obtained by heating KH$_2$PO$_4$ (Aldrich, 99.995%) for 5 h at 300° C in air. The reactants were ground thoroughly, pelletized, and fired at 550° C for 48 h in flowing argon atmosphere with intermediate grindings. The phase purity of the sample was confirmed by powder x-ray diffraction (XRD) measurement at room temperature using a PANalytical powder diffractometer (CuK_α radiation, $\lambda_{\rm avg} \simeq 1.5418$ Å).

Figure 2 shows the powder XRD pattern at room temperature. Rietveld refinement of the acquired XRD data was performed using the FULLPROF software package [23]. The initial structure parameters were taken from Ref. [21]. All the peaks could be fitted using the pseudo-Voigt function. The best fit was obtained with a goodness of fit $\chi^2 \simeq 3.4$. The obtained lattice parameters [$a = 12.7612(2)$ Å, $b = 6.3658(2)$ Å, $c = 10.5052(1)$ Å, and $V_{\rm cell} = 853.40(4)$ Å^3] are in close agreement with the previous report [21].

Magnetization (M) was measured as a function of temperature (2.1 K $\leqslant T \leqslant$ 380 K) and magnetic field (H) using the vibrating sample magnetometer (VSM) attachment to the physical property measurement system [PPMS, Quantum Design]. High-field magnetization was measured in pulsed magnetic field at the Dresden high magnetic field laboratory [24,25]. Specific heat ($C_{\rm p}$) as a function of temperature was measured down to 0.35 K using the thermal relaxation technique in PPMS by varying magnetic field from 0 to 14 T. For $T \leqslant 2$ K, measurements were performed using an additional ^{3}He attachment to PPMS.

The NMR measurements were carried out using pulsed NMR techniques on ^{31}P (nuclear spin $I = 1/2$ and gyromagnetic ratio $\gamma_N/2\pi = 17.235$ MHz/T) nuclei in the temperature range 1.8 K $\leqslant T \leqslant$ 250 K. The NMR measurements were done at a radio frequency of 24.76 MHz. Spectra were obtained by sweeping the magnetic field at a fixed frequency. The NMR shift $K(T) = \Delta H/H = [H_{\rm ref} - H(T)]/H(T)$ was determined by measuring the resonance field of the sample [$H(T)$] with respect to the nonmagnetic reference H$_3$PO$_4$ (resonance field $H_{\rm ref}$). The ^{31}P spin-lattice relaxation rate $1/T_1$ was measured as a function of temperature using the inversion recovery method.

Neutron powder diffraction (NPD) measurements [26] were carried out at various temperatures down to 1.5 K using the time-of-flight diffractometer WISH at the ISIS Facility, UK [27]. The Rietveld refinements of the NPD data were executed using the FULLPROF software package [23].

Density-functional-theory (DFT) band-structure calculations were performed in the FPLO code [28] using Perdew-Burke-Ernzerhof (PBE) flavor of the exchange-correlation potential [29]. Correlation effects in the V 3d shell were taken into account on the mean-field level (DFT + U) with the on-site Coulomb repulsion $U_d = 3$ eV, Hund's coupling $J_d = 1$ eV, and double-counting correction in the atomic limit [30]. Exchange couplings entering the spin Hamiltonian

$$\mathcal{H} = \sum_{\langle ij\rangle} J_{ij}\mathbf{S}_i\mathbf{S}_j, \tag{1}$$

where $S = \frac{1}{2}$ and the summation is over bonds $\langle ij\rangle$, were obtained by a mapping procedure from the total energies of collinear spin configurations [31,32]. Alternatively, we used the superexchange theory of Refs. [33,34], as further explained in Sec. III E.

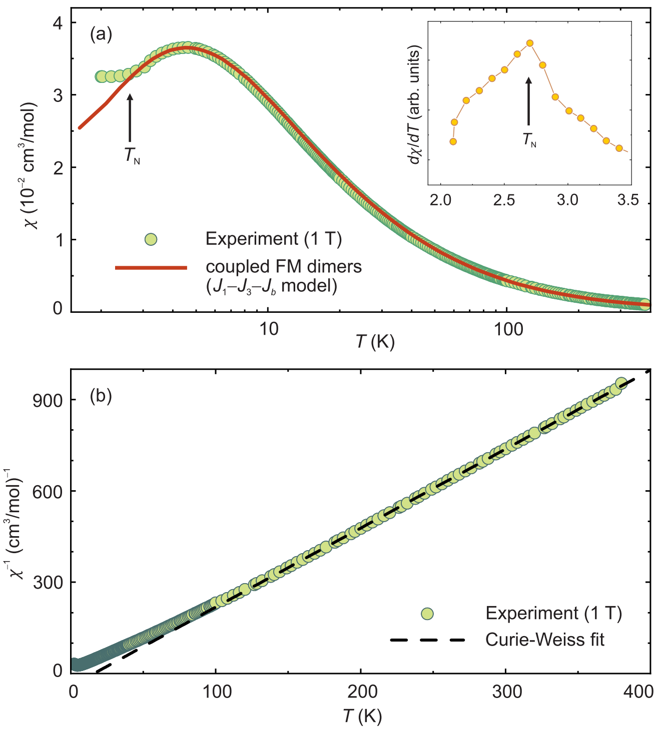

FIG. 3. (a) Magnetic susceptibility $\chi(T)$ measured in the applied field of $\mu_0H = 1$ T. The solid line is the fit with the model of coupled FM dimers with $J_1 = -150$ K, $J_3 = 12$ K, and $J_b = 1.5$ K [see also Fig. 12(c) and Sec. III E]. Inset: $d\chi/dT$ vs T. (b) Inverse susceptibility $(1/\chi)$ as a function of temperature and the CW fit using Eq. (2).

Quantum Monte Carlo (QMC) simulations were performed using the LOOP [35] and DIRLOOP_SSE [36] algorithms of the ALPS package [37] on the $L \times L/2$ finite lattices with periodic boundary conditions and $L \leqslant 36$. The spin lattice used in the simulations is detailed in Sec. III E.

III. RESULTS

A. Magnetization

The magnetic susceptibility $\chi(T)$ [$\equiv M(T)/H$] measured in an applied field of $\mu_0H = 1$ T is displayed in Fig. 3(a). With decreasing temperature, $\chi(T)$ increases in a Curie-Weiss (CW) manner, as expected in the high-temperature regime, and then passes through a broad maximum at $T_\chi^{\max} \simeq 5$ K, indicative of an AFM short-range order. These features are independent of the applied field. A small kink at $T_N \simeq 2.7$ K indicates the magnetic ordering transition, which is more pronounced in the $(d\chi/dT)$ versus T plot shown in the inset [38]. In contrast to the other $AVOXO_4$ compounds with the prominent Curie tail below 5–10 K [14,19], the low-temperature susceptibility of α-KVOPO$_4$ saturates at a constant value and provides testimony to the high quality of the polycrystalline sample with a negligible amount of paramagnetic impurities and/or defects.

The $\chi(T)$ data in the paramagnetic (PM) region were fitted with the Curie-Weiss law

$$\chi(T) = \frac{C}{T - \theta_{\mathrm{CW}}}, \tag{2}$$

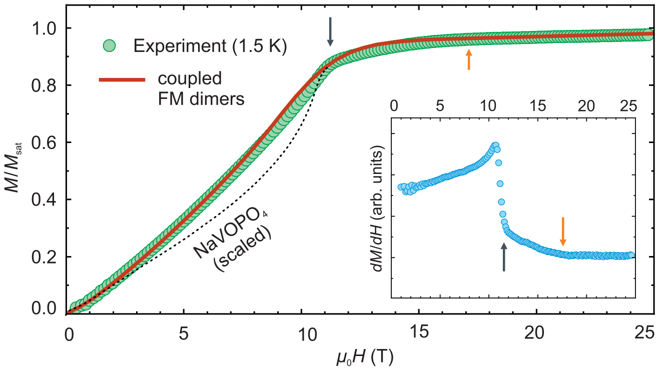

FIG. 4. Magnetization vs field measured at $T = 1.5$ K and the fit with the model of coupled FM dimers (J_1–J_3–J_b) using the same parameters as in Fig. 3. The dotted line shows the magnetization curve of NaVOPO$_4$ [17] scaled to the same H_s for an easier comparison. The inset shows dM/dH vs H. The colored arrows indicate the field range above $\mu_0H_s \simeq 11.3$ T where the residual curvature of $M(H)$ is observed (see text for details).

where C is the Curie constant and θ_{CW} is the Curie-Weiss temperature. The fit above 150 K [see Fig. 3(b)] returns $C \simeq 0.386$ cm^{3}K/mol and $\theta_{\mathrm{CW}} \simeq 15.9$ K. The C value corresponds to the paramagnetic effective moment of 1.756 μ_{B}, which is similar to 1.73 μ_B expected for spin-$\frac{1}{2}$. More interestingly, the positive Curie-Weiss temperature signals predominant FM couplings despite the susceptibility maximum above T_N and the associated short-range AFM order, which is typical for low-dimensional antiferromagnets.

The magnetization curve measured in pulsed magnetic fields up to 60 T at the base temperature of 1.5 K (Fig. 4) approaches saturation around 12 T. This field defines the energy required to overcome AFM interactions and polarize the spins. It serves as a witness for AFM couplings that are nevertheless weaker than the FM ones. Interestingly, the magnetization curve is nearly linear. Its curvature is smaller than in the other low-dimensional V^{4+} magnets [7,24], including the $AVOXO_4$ compounds with A = Li, Na, and Ag [15–17]. We illustrate this in Fig. 4 by showing the scaled magnetization curve for NaVOPO$_4$ as the reference for a low-dimensional V^{4+} antiferromagnet. Along with the FM Curie-Weiss temperature, the reduced curvature of $M(H)$ sets α-KVOPO$_4$ apart from other V^{4+} materials with the similar composition.

Another peculiarity of α-KVOPO$_4$ is its behavior near saturation, where a residual curvature is observed above the kink at $\mu_0H_s \simeq 11.3$ T before $M(H)$ becomes completely flat around 17 T (Fig. 4, inset). Similar features were reported in BaCdVO(PO$_4$)$_2$ [39–41] and assigned to a spin-nematic state expected in a strongly frustrated square-lattice antiferromagnet in the vicinity of saturation [42]. However, in the α-KVOPO$_4$ case a more trivial explanation, the distribution of saturation fields depending on the field direction, could be an equally plausible reason for the residual curvature above H_s. It is also possible that a chemical inhomogeneity related to the mobile K atoms leads to a distribution of the saturation fields. High atomic displacement parameters of potassium [20,21] indeed suggest a distribution of the K atoms around their ideal sites. On the other hand, the scenario of K deficiency can be excluded because it would change the oxidation state

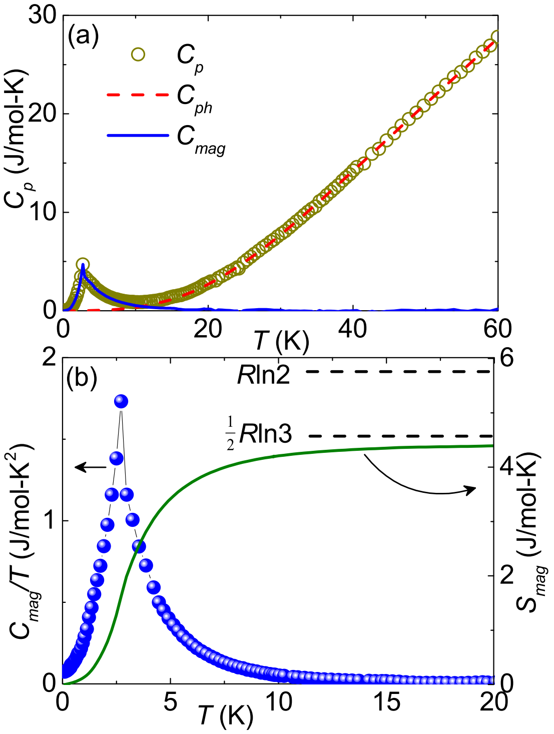

FIG. 5. (a) Specific heat (C_p) vs T for α-KVOPO$_4$ in zero applied field. The dashed red line is the phonon contribution to the specific heat (C_{ph}) determined using Debye fit [Eq. (3)]. The solid blue line indicates the magnetic contribution to the specific heat C_{mag}. (b) C_{mag}/T and S_{mag} vs T in the left and right y-axes, respectively.

of vanadium, whereas the value of the paramagnetic effective moment suggests pure V^{4+} in our sample.

B. Specific heat

The specific heat (C_p) measured in zero magnetic field is shown in Fig. 5(a). In the high-temperature region, $C_p(T)$ is entirely dominated by phonon excitations, whereas at low temperatures magnetic contribution becomes prominent. The λ-type anomaly at $T_N \simeq 2.7$ K confirms the magnetic transition.

Magnetic contribution C_{mag} was separated by subtracting the estimated phonon contribution (C_{ph}) from the total measured $C_p(T)$. To this end, the data above 40 K were fitted by a linear combination of four Debye functions [43,44]

$$C_{ph}(T) = 9R\sum_{n=1}^{4} c_n\left(\frac{T}{\theta_{Dn}}\right)^3 \int_0^{\frac{\theta_{Dn}}{T}} \frac{x^4e^x}{(e^x-1)^2}dx. \qquad (3)$$

Here, R is the universal gas constant, the coefficients c_n represent the number of distinct atoms in the formula unit, and θ_{Dn} are the corresponding Debye temperatures. The resulting C_{mag} and the respective magnetic entropy S_{mag} obtained by integrating $C_{mag}(T)/T$ [Fig. 5(b)] suggest that about 75% of the total magnetic entropy $R\ln 2 = 5.76$ J/mol K is released below 10 K. This value is remarkably close to $\frac{1}{2}R\ln 3 = 4.56$ J/mol K that can be indicative of the $S = 1$ magnetic units formed by pairs of ferromagnetically coupled spin-$\frac{1}{2}$ V^{4+} ions, as we show below. Additional magnetic entropy beyond $\frac{1}{2}R\ln 3$ should be released at higher temperatures, but it is difficult to extract because the phonon term becomes predominant.

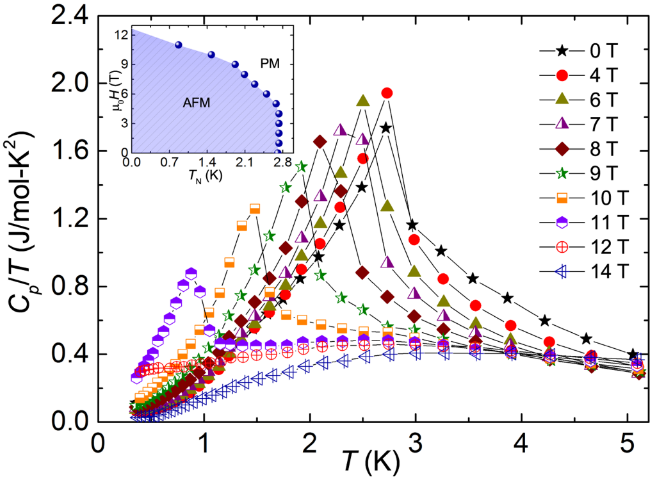

FIG. 6. Specific heat divided by temperature (C_p/T) vs T for α-KVOPO$_4$ measured in different fields in the low-T regime. Inset: H vs T_N phase diagram.

We also followed the evolution of T_N in the applied field in Fig. 6. From the H vs T_N phase diagram (inset of Fig. 6), it is evident that the transition temperature is nearly unchanged up to 4 T and decreases gradually in higher fields. Such a behavior is intermediate between classical antiferromagnets, where T_N is systematically reduced by the field [45], and low-dimensional quantum antiferromagnets, where T_N initially increases and then becomes suppressed, thus leading to a nonmonotonic phase boundary [46,47]. The absence of such a nonmonotonic phase boundary, despite the presence of the susceptibility maximum due to short-range order, also distinguishes α-KVOPO$_4$ from a typical low-dimensional spin-$\frac{1}{2}$ antiferromagnet.

C. ^{31}P NMR

1. NMR spectra

The α-KVOPO$_4$ structure contains two nonequivalent P (P1 and P2) sites and both of them are coupled to the V^{4+} ions in each chain. Both the P sites reside in an almost symmetric position between the four V^{4+} ions connecting two (V1–V2) dimers. ^{31}P being a $I = 1/2$ nucleus, one expects a single and narrow spectral line for each of the P sites.

Figure 7 presents the ^{31}P NMR spectra measured at different temperatures. We observed a single spectral line at high temperatures, but the line shape is found to be asymmetric, similar to that observed in Zn$_2$VO(PO$_4$)$_2$ and Sr(TiO)Cu$_4$(PO$_4$)$_4$ [48,49]. The single spectral line implies that both the P-sites are almost equivalent or have the same local environment. Further, the asymmetric line shape is likely due to the anisotropy in $\chi(T)$ and/or asymmetric hyperfine coupling between the ^{31}P nuclei and V^{4+} spins. With the decrease in temperature, the line broadens drastically with a pronounced shoulder on the high-field side. This shoulder becomes a peak with almost equal intensity as that of the low-field peak. Both peaks shift as we lower the temperature.

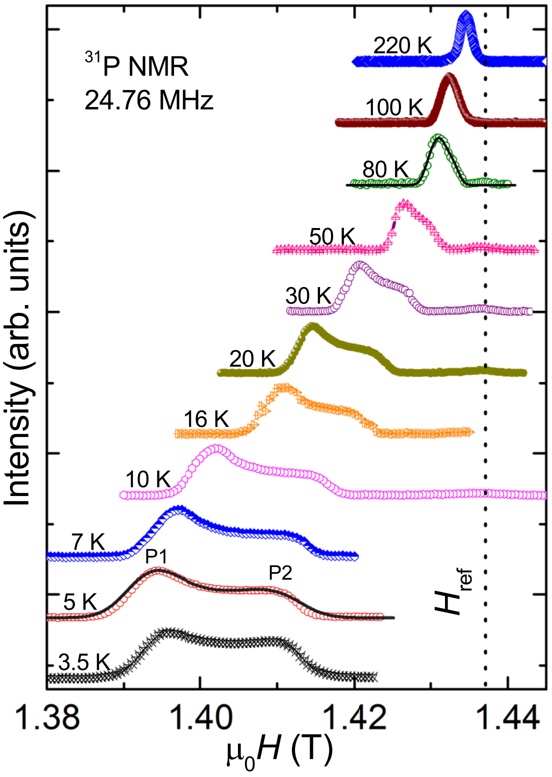

FIG. 7. Field-sweep ^{31}P NMR spectra at different temperatures (for $T > T_N$) measured at 24.76 MHz. The vertical dashed line corresponds to the ^{31}P resonance frequency of the reference sample H_3PO_4. The solid lines are the fits to the spectra at $T = 80$ K and 5 K, taking into account one (P1) and two (P1 and P2) P sites, respectively.

This suggests that the local environment of P changes slightly and that the two P sites experience different local fields at low temperatures. At very low temperatures, when the system approaches T_N, the spectra broaden abruptly.

In spherical polar coordinates, the relative shift of the NMR line in terms of the K-tensor can be written as [50]

$$\frac{\Delta H}{H} = K_{\text{iso}} + K_{\text{ax}}(3\cos^2\theta - 1) + K_{\text{aniso}}\sin^2\theta\cos 2\phi. \quad (4)$$

Here, the anisotropic components of the NMR shift tensor are defined as $K_{\text{iso}} = \frac{1}{3}(K_{xx} + K_{yy} + K_{zz})$, $K_{\text{ax}} = \frac{1}{6}(2K_{zz} - K_{xx} - K_{yy})$, and $K_{\text{aniso}} = \frac{1}{2}(K_{yy} - K_{xx})$. The spectra in Fig. 7 could be fitted by Eq. (4) taking into account only one P site down to 35 K. Below 35 K, the whole spectra could only be fitted by accounting for the superposition of two P sites. A small discrepancy between the simulated and the experimental spectra can be attributed to the effect of partial grain reorientations with respect to the external field and/or anisotropic spin-spin relaxation time.

2. NMR shift

Anisotropic components of the NMR shift as a function of T estimated by fitting each spectrum are presented in Figs. 8(a) and 8(b) for both the P sites. With the decrease in temperature, the isotropic NMR shift (K_{iso}) of both the P sites increases in a CW manner and then shows a broad maximum around 5 K, similar to $\chi(T)$. Unlike bulk $\chi(T)$, $K(T)$ is insensitive to free spins and defects and allows a more reliable estimate of the intrinsic susceptibility.

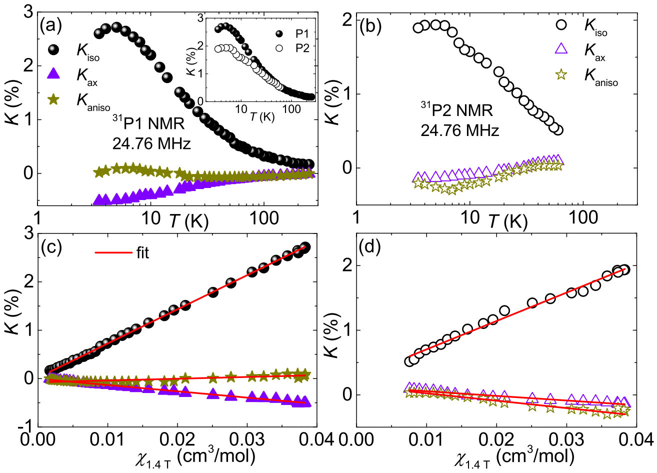

FIG. 8. NMR shift components (K_{iso}, K_{ax}, and K_{aniso}) for the (a) P1 and (b) P2 sites as a function of T. K vs χ measured at 1.4 T is plotted with temperature as an implicit parameter for (c) P1 and (d) P2 sites. The solid lines are the linear fits as described in the text. Inset of (a): K_{iso} of both the P sites are plotted as a function of T for a comparison.

The relation between $K(T)$ and $\chi(T)$ is typically written as

$$K(T) = K_0 + \frac{A_{\text{hf}}}{N_A}\chi_{\text{spin}}(T), \quad (5)$$

where K_0 is the temperature-independent chemical shift, A_{hf} is the hyperfine coupling constant between the ^{31}P nuclei and V^{4+} electronic spins, and $\chi_{\text{spin}}(T)$ is the intrinsic susceptibility. As shown in Figs. 8(c) and 8(d) the K versus bulk χ plots are linear over the whole measured temperature range, i.e., 3.5 K to 250 K for P1 and 3.5 K to 60 K for P2. From the slope of the linear fits we determine [$A_{\text{hf}}^{\text{iso}}(P1) \simeq 0.39$ T/μ_B, $A_{\text{hf}}^{\text{ax}}(P1) \simeq -0.07$ T/μ_B, and $A_{\text{hf}}^{\text{aniso}}(P1) \simeq 0.02$ T/μ_B] and [$A_{\text{hf}}^{\text{iso}}(P2) \simeq 0.24$ T/μ_B, $A_{\text{hf}}^{\text{ax}}(P2) \simeq -0.04$ T/μ_B, and $A_{\text{hf}}^{\text{aniso}}(P2) \simeq -0.06$ T/μ_B] for the P1 and P2 sites, respectively. These values of $A_{\text{hf}}^{\text{iso}}$ are comparable with the values reported for other transition-metal phosphate compounds [17,51,52].

3. Spin-lattice relaxation rate $1/T_1$

The local spin-spin correlations can be understood by measuring the temperature-dependent spin-lattice relaxation rate $1/T_1$, which yields information on the imaginary part of the dynamic susceptibility $\chi(q, \omega)$. The ^{31}P $1/T_1$ was measured by exciting the sample at the field corresponding to the peak/shoulder positions down to $T = 2$ K. As expected, the recovery of the longitudinal magnetization follows the single-exponential behavior, which is typical for a $I = 1/2$ nucleus. The longitudinal recovery curves at various temperatures were fitted well by the single exponential function

$$\frac{1}{2}\left[1 - \frac{M(t)}{M(0)}\right] = Ae^{-t/T_1} + C. \quad (6)$$

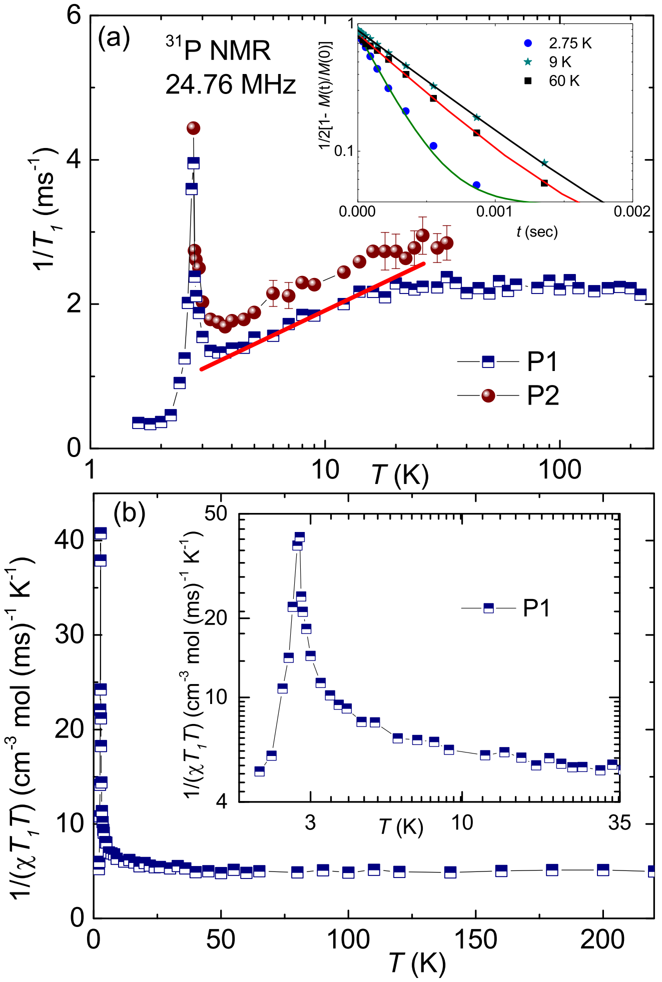

FIG. 9. (a) Spin-lattice relaxation rate $1/T_1$ vs T measured at 24.96 MHz at the two shoulder positions. Solid line depicts the linear behavior for $T \leqslant 20$ K. Inset: Recovery of the longitudinal magnetization as a function of t for three different temperatures. Solid lines are fits using Eq. (6). (b) Plot of $1/(\chi T_1 T)$ vs T using $1/T_1$ of the low-field shoulder (P1). Inset: The low-T $1/(\chi T_1 T)$ data are magnified.

Here, $M(t)$ is the nuclear magnetization at a time t after the inversion pulse, $M(0)$ is the equilibrium magnetization, and C is a constant. Recovery curves at three different temperatures along with the fit are shown in the inset of Fig. 9(a).

As shown in Fig. 7, the NMR spectra are asymmetric with two shoulders corresponding to two P sites. In view of this, we measured $1/T_1(T)$ at both shoulder positions and the data are shown in Fig. 9(a). The overall behavior of $1/T_1(T)$ for both the P-sites are nearly the same, except for a small change in magnitude. With decreasing temperature, $1/T_1$ remains constant down to 20 K due to fluctuating paramagnetic moments [53]. With a further decrease in temperature, $1/T_1$ decreases in a linear manner and then exhibits a sharp peak at $T_N \simeq 2.72$ K. This sharp peak at T_N reflects the slowing down of the fluctuating moments upon approaching T_N. Below T_N, $1/T_1$ gradually decreases toward zero. It is reflected from the $\chi(T)$ and $K(T)$ data that the AFM correlations start to grow below 25 K. As both the P sites are positioned almost symmetrically between two FM V1–V2 dimers with opposite spins, the staggered ($q = \pm\pi/a$) fluctuations from the V^{4+} spins get filtered out partially at the P-site. This leads to a linear decrease of $1/T_1$ below 20 K, as the AFM correlations are built in. Typically, similar behavior is observed in AFM spin-1/2 chains in the temperature regime $T \sim J/k_B$, where $1/T_1$ is dominated by the uniform $q = 0$ fluctuations [51,54].

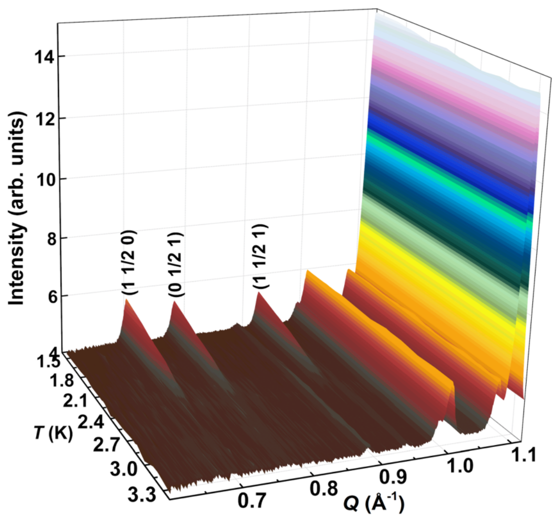

FIG. 10. Temperature evolution of the neutron powder diffraction patterns of α-KVOPO$_4$ in the low-Q regime and for temperatures below 3.4 K. An emergence of magnetic reflections with $\mathbf{k} = (0, \frac{1}{2}, 0)$ is evident below T_N.

In Fig. 9(b), $1/(\chi T_1 T)$ is plotted against T. At high temperatures, it is almost temperature-independent and then increases slowly below about 25 K. In the inset of Fig. 9(b), the data near T_N are magnified to highlight this slow increase. The general expression for $\frac{1}{T_1 T}$ in terms of the dynamic susceptibility $\chi_M(\vec{q}, \omega_0)$ can be written as [53,55]

$$\frac{1}{T_1 T} = \frac{2\gamma_N^2 k_B}{N_A^2} \sum_{\vec{q}} |A(\vec{q})|^2 \frac{\chi''(\vec{q}, \omega_0)}{\omega_0}, \tag{7}$$

where the sum is over the wave vector $\vec{q}$ within the first Brillouin zone, $A(\vec{q})$ is the form factor of the hyperfine interaction, and $\chi''(\vec{q}, \omega_0)$ is the imaginary part of the dynamic susceptibility at the nuclear Larmor frequency ω_0. For $q = 0$ and $\omega_0 = 0$, the real component of $\chi'(\vec{q}, \omega_0)$ represents the uniform static susceptibility (χ). Thus, the temperature-independent $1/(\chi T_1 T)$ in the high-temperature region ($\geqslant$25 K) indicates the dominant contribution of χ to $1/T_1 T$. Thus, the slow increase below 25 K can be attributed to the growth of AFM correlations.

D. Neutron diffraction

We now probe the magnetic order using neutron diffraction. Figure 10 shows that a set of magnetic reflections develop below T_N with the strongest reflections at $Q = 0.6973$ Å^{-1}, 0.7757 Å^{-1}, and 0.9189 Å^{-1}. They can be indexed with the propagation vector $\mathbf{k} = (0, \frac{1}{2}, 0)$ suggesting a commensurate magnetic order.

The Rietveld refinement was done using the total diffracted intensities at different temperatures. All the five banks of data

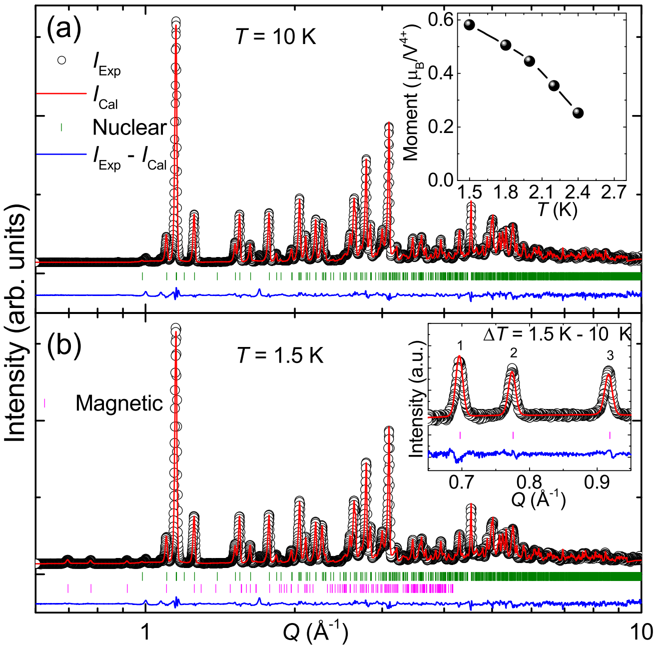

FIG. 11. The neutron powder diffraction patterns along with the Rietveld refinement for (a) $T = 10$ K and (b) $T = 1.5$ K. Open black circles represent the experimental data, red solid line represents the calculated curve, and difference between them is shown as a blue solid line at the bottom. Vertical marks correspond to the position of all allowed Bragg peaks for the nuclear (top row) and magnetic (bottom row) reflections. The inset in (a) shows the temperature variation of ordered magnetic moment. Inset in (b) presents the Rietveld refinement of the difference data ($\Delta T = 1.5$–10 K) using only the magnetic model.

have been refined simultaneously to obtain the final parameters. Figure 11(a) represents the Rietveld refinement of the nuclear pattern at $T = 10$ K using the orthorhombic crystal structure with the space group $Pna2_1$ [56]. The obtained lattice parameters are $a = 12.7521(3)$ Å, $b = 6.3603(2)$ Å, $c = 10.4985(2)$ Å, and $V_{\rm cell} = 851.52(3)$ Å^3. These values are in close agreement with the refined values from the powder XRD data at room temperature [21]. A tiny extra peak at $Q \simeq 1.7$ Å^{-1} corresponds to a small nonmagnetic impurity phase of KPO$_3$ in the polycrystalline sample.

Magnetic structure refinement was performed for the diffraction data from the paired detector banks 2 and 9 [27] with the average scattering angle $2\theta \simeq 58.3^\circ$. This diffraction pattern covers the relevant low-Q range, containing all magnetic reflections, with the best resolution [57]. Figure 11(b) shows the combined Rietveld refinement of the nuclear and magnetic reflections at $T = 1.5$ K. The refinement was assisted by the symmetry analysis performed using ISODISTORT [58] and ISOTROPY [59] software. The only irreducible representation (mY_1) associated with the $k = (0, 1/2, 0)$ propagation vector is two-dimensional and yields three possible magnetic space groups: P_bc (No. 7.29), P_a2_1 (No. 4.10), and P_S1 (No. 1.3). They correspond to the $(a, 0)$, (a, a), and (a, b) order parameter directions, respectively. A solution was found in the magnetic space group P_bc with the basis vectors (0,0,1), (0,2,0), $(-1, 0, 0)$ and origin at $(0, 1/4, 0)$ with respect to the paramagnetic $Pna2_1$ space group. Although the magnetic space group implies four symmetry-independent V sites, in the final refinement all sites were constrained to be collinear and have equal magnitude of the magnetic moments to avoid correlations and reduce the number of fitting parameters. The magnetic moments lie in the ac-plane with $\mu_a = 0.53(5)\ \mu_B$ and $\mu_c = 0.23(8)\ \mu_B$ at 1.5 K. The spin arrangement is shown in Fig. 12 and will be discussed in detail in the next section along with the relevant magnetic couplings.

E. Microscopic magnetic model

To analyze magnetic couplings in α-KVOPO$_4$, we first consider band dispersions and associated hopping parameters in the band structure obtained on the PBE level without taking strong correlations into account. Band structures of the V^{4+} compounds usually show a well-defined crystal-field splitting imposed by the local environment of vanadium with the short vanadyl bond toward one of the oxygen atoms. This short bond defines the local z-direction and renders d_{xy} the lowest-energy, half-filled magnetic orbital. The d_{xy} bands around the Fermi level are typically well separated from the higher-lying bands formed by the four remaining d-orbitals [60,61].

An inspection of the α-KVOPO$_4$ band structure (Fig. 13) suggests a small but important deviation from this conventional scenario. The band complex between -0.2 and 0.2 eV includes 12 bands per 8 V atoms, so it cannot be formed by the d_{xy} states only. An orbital-resolved density of states reveals that these bands include the majority of the d_{xy} contribution, but also a significant portion of the d_{yz} and d_{xz} states. Their admixture is caused by the remarkably large xy–yz and xy–xz hoppings of 0.25–0.30 eV for the V–V pairs with the 3.412 Å separation (J_1 bond).

We now use Wannier projections to construct a five-orbital tight-binding model that reproduces all V 3d bands, and introduce the extracted hoppings into the superexchange theory [33,34] that yields magnetic couplings as

$$J = \frac{4t_{xy}^2}{U_{\rm eff}} - \sum_\alpha \frac{4\,t_{xy\to\alpha}^2\,J_{\rm eff}}{(U_{\rm eff}+\Delta_\alpha)(U_{\rm eff}+\Delta_\alpha-J_{\rm eff})}, \qquad (8)$$

where t_{xy} are the hoppings between the half-filled (d_{xy}) orbitals, $t_{xy\to\alpha}$ are the hoppings between the half-filled and empty orbitals, the index α goes through these empty d-orbitals, Δ_α are the corresponding crystal-field splittings, $U_{\rm eff} = 3$ eV is the effective Coulomb repulsion, and $J_{\rm eff} = 1$ eV is the effective Hund's coupling. The first and second terms of Eq. (8) stand, respectively, for the AFM ($J^{\rm AFM}$) and FM ($J^{\rm FM}$) contributions to the exchange, as listed in Table I.

The large xy–yz and xy–xz hoppings on the J_1 bond render the respective magnetic coupling strongly FM. This coupling is augmented by a much weaker AFM J_3, whereas all other couplings are below 5–7 K in magnitude, either FM or AFM. Our DFT + U mapping analysis (Table I) leads to essentially similar results, with the leading FM coupling J_1 and the secondary AFM coupling J_3. One immediate and rather unexpected consequence of this analysis is that the structural chains with the alternating V–V separations of 3.415 Å (J_1) and 3.520 Å (J_2), as shown in Fig. 1(b), break into FM dimers formed by the previous bond. On the other hand, J_2 features

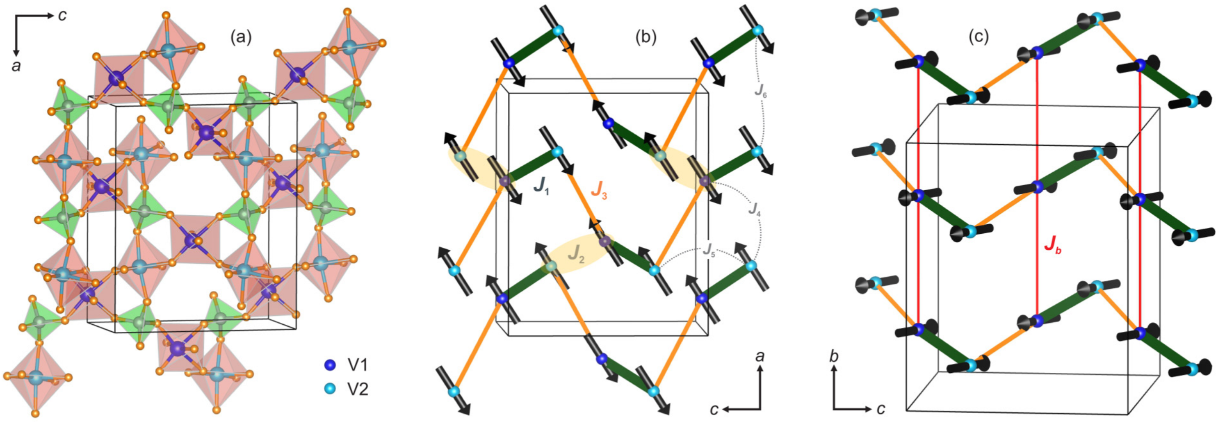

FIG. 12. (a),(b) Crystal and magnetic structures of α-KVOPO$_4$ shown in the same projection, with the K atoms omitted for clarity. The shadings in panel (b) highlight the J_2 bonds with the parallel and antiparallel spin arrangement, thus illustrating that J_2 does not stabilize the magnetic order. (c) The coupling J_b connects the J_1–J_3 chains into layers and causes antiferromagnetic order along b with $\mathbf{k} = (0, \frac{1}{2}, 0)$.

weak FM and AFM contributions that nearly compensate each other. Indeed, the FM dimers of J_1 can be clearly distinguished in the experimental magnetic structure. In contrast, the spins on the J_2 bonds are both parallel and antiparallel [Fig. 12(b)], thus indicating that J_2 does not contribute to the stabilization of the long-range order.

The two leading couplings, J_1 and J_3, form bond-alternating spin chains with the strong FM and weak AFM couplings [Fig. 12(b)]. Experimental magnetic structure suggests that neither J_2 nor J_4–J_6 stabilize the order between these chains. The most likely candidate for the interchain coupling is then J_b, which runs along the crystallographic b direction and is also responsible for the doubling of the magnetic unit cell [Fig. 12(c)]. Our DFT results indeed show a small J_b, although between the V1 sites only, whereas the respective interaction between the V2 sites should be below 0.1 K and thus negligible. The interactions J_b couple the aforementioned alternating spin chains into layers. Long-range magnetic order between these layers may be caused by residual interactions, which are too weak to be resolved in DFT, or by minute anisotropic terms in the spin Hamiltonian.

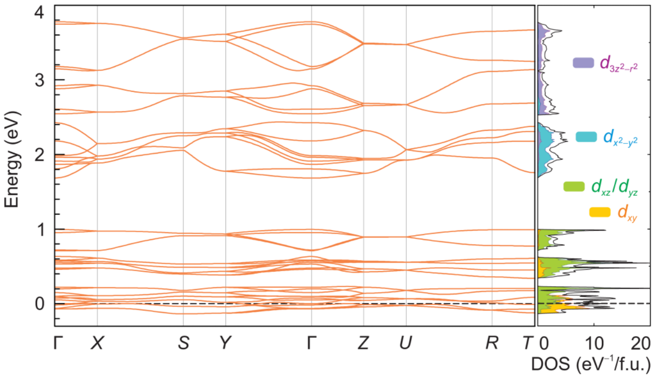

FIG. 13. Energy bands and the corresponding density of states (DOS) obtained from the PBE calculation for α-KVOPO$_4$. The Fermi level is at zero energy. Note the crystal-field splitting of the V $3d$ states with the significant mixing of d_{xy} and d_{yz}/d_{xz} around the Fermi level.

While these weak interlayer interactions and/or anisotropy require further dedicated analysis, we argue that the J_1–J_3–J_b model of coupled bond-alternating spin chains reproduces the main features of the experimental data. To this end, we simulate thermodynamic properties by QMC and find an excellent agreement with both $\chi(T)$ (Fig. 3) and $M(H)$ (Fig. 4) using the same set of parameters: $J_1 = -150$ K, $J_3 = 12$ K, $J_b = 1.5$ K, and $g = 1.98$. Further on, we estimate the zero-temperature ordered magnetic moment μ_0 by calculating the spin structure factor $S(\mathbf{k})$ for the same set of exchange parameters and using the finite-size scaling for the staggered magnetization [62]

$$m_s(L)^2 = \mu_0^2 + \frac{m_1}{L} + \frac{m_2}{L^2}, \tag{9}$$

where L is the size of the finite lattice and m_1 and m_2 are empirical parameters. The resulting $\mu_0 \simeq 0.68\ \mu_B$ (Fig. 14) reveals the 32% reduction compared to the classical value of 1 μ_B. Experimental values of the ordered moment are even lower and affected by thermal fluctuations because the base temperature of our neutron diffraction measurement is more than half of T_N. From the empirical scaling, $\mu(T) = \mu_0[1 - (T/T_N)^\alpha]^\beta$, we estimate $\mu_0^{\text{exp}} = 0.66\ \mu_B$ in an excellent agreement with QMC (Fig. 14, inset).

TABLE I. Interatomic V–V distances (in Å) and the corresponding exchange couplings (in K) calculated using superexchange theory [J^{AFM} and J^{FM} from Eq. (8)] and mapping analysis ($J^{\text{DFT}+U}$). The V–V distances are given using the structural parameters from Ref. [21]. The couplings not listed in this table are well below 1 K.

	$d_{\text{V-V}}$		J^{AFM}	J^{FM}	$J^{\text{DFT}+U}$
J_1	3.415	V1–V2	0	−154	−149
J_2	3.520	V1–V2	16	−9	−3
J_3	5.622	V1–V2	34	−4	17
J_4	5.731	V1–V2	1	0	−3
J_5	6.138	V2–V2	4	−2	1
J_b	6.360	V1–V1	5	−4	1
J_6	6.376	V2–V2	2	−3	−2

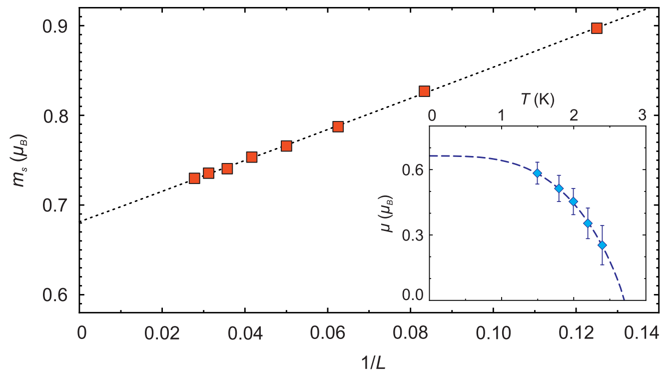

FIG. 14. Finite-size scaling of the staggered magnetization (m_s) obtained from the static structure factor calculated by QMC at $\beta = 1/(k_BT) = 16L$. The dashed line is the fit with Eq. (9). The inset shows the experimental ordered magnetic moment (μ) as a function of temperature and its empirical extrapolation, as described in the text.

IV. DISCUSSION AND SUMMARY

Weak FM couplings are not uncommon among the V^{4+} compounds. They usually take place between those ions where magnetic d_{xy} orbitals lie in parallel, well-separated planes and lack a suitable superexchange pathway [14]. However, more efficient superexchange pathways are always found for other pairs of the V^{4+} ions and give rise to AFM couplings of a similar or even higher strength. α-KVOPO$_4$ stands as an exception in this row because its FM coupling $J_1 \simeq -150$ K is by far the strongest among the known V^{4+} compounds and, therefore, predominant. It arises between the d_{xy} orbitals lying in nonparallel, nearly orthogonal planes and can be traced back to the effective orbital order between the two distinct vanadium sites in the crystal structure, V1 and V2 [Fig. 1(b)]. One interesting question in this respect is why the strong FM coupling is observed for J_1 and not for J_2, despite the similar V–V distances. This difference can be traced back to the dihedral angles ψ between the planes of the d_{xy} orbitals ($\psi = 30.4^\circ$ for J_1 and 35.5° for J_2) and to the additional superexchange pathways that arise from the PO$_4$ bridges.

As a system dominated by FM couplings, α-KVOPO$_4$ is not expected to show any significant quantum effects. Nevertheless, several experimental observations—the susceptibility maximum preceding T_N, and the reduction in the ordered magnetic moment—challenge these expectations. Our model of weakly coupled FM dimers reproduces all significant features of the experimental data and suggests weak AFM couplings J_3 and J_b as the origin of the quantum effects in α-KVOPO$_4$. The separation of energy scales into strong FM $J_1 = -150$ K and weak AFM $J_3 = 12$ K further implies that at low temperatures an effective description in terms of $S = 1$ moments located on the J_1 dimers may be appropriate. This description is supported by the magnetic entropy of 4.3 J/mol K released below 10 K and corresponding to $\frac{1}{2}R\ln 3 = 4.56$ J mol K for 0.5 $S = 1$ dimers per formula unit. The effective $S = 1$ description entails $S = 1$ Haldane chains formed by J_3 and coupled into layers by J_b. Such coupled $S = 1$ chains show a quantum phase transition between the magnetically ordered and gapped Haldane phases [63,64]. The proximity to this transition may give a further clue to the reduced ordered moment and quantum effects in α-KVOPO$_4$.

In summary, α-KVOPO$_4$ is an unusual spin-$\frac{1}{2}$ magnet featuring strong FM and weak AFM couplings. While the FM couplings cause the formation of ferromagnetic spin dimers, the AFM ones connect these dimers into layers and trigger quantum effects. Quantum fluctuations manifest themselves by the short-range order that appears below 5 K and precedes the long-range order formed at $T_{\mathrm{N}} = 2.7$ K. Below T_{N}, the commensurate and collinear ground state features a strongly reduced ordered magnetic moment of 0.58 μ_B at 1.5 K. The unusually strong FM coupling J_1 is caused by the effective orbital order on the two crystallographically nonequivalent vanadium sites. Overall, from the magnetism perspective α-KVOPO$_4$ is entirely different from its siblings, such as NaVOPO$_4$ with its field-induced quantum critical point [17] and AgVOAsO$_4$ with the double-dome regime of magnon BEC [15]. The remarkable structural diversity of the V^{4+} phosphates with their different connectivities of the vanadium polyhedra [65] suggests that further unusual regimes of magnetic couplings may occur in this broad family of compounds.

ACKNOWLEDGMENTS

P.K.M., K.S., and R.N. acknowledge SERB, India for financial support bearing sanction order No. CRG/2019/000960. We also acknowledge the support of the HLD at HZDR, member of European Magnetic Field Laboratory (EMFL). Thanks to ISIS facility for neutron beam time on the WISH beamline (RB2000205).

---

[1] P. W. Anderson, Theory of magnetic exchange interactions: Exchange in insulators and semiconductors, in *Solid State Physics* (Elsevier, New York, 1963), Vol. 14, pp. 99–214.

[2] K. Hasegawa, M. Isobe, T. Yamauchi, H. Ueda, J. I. Yamaura, H. Gotou, T. Yagi, H. Sato, and Y. Ueda, Discovery Of Ferromagnetic-Half-Metal-To-Insulator Transition In K$_2$Cr$_8$O$_{16}$, Phys. Rev. Lett. **103**, 146403 (2009).

[3] P. Mahadevan, A. Kumar, D. Choudhury, and D. D. Sarma, Charge Ordering Induced Ferromagnetic Insulator: K$_2$Cr$_8$O$_{16}$, Phys. Rev. Lett. **104**, 256401 (2010).

[4] D. I. Khomskii and K. I. Kugel, Orbital and magnetic structure of two-dimensional ferromagnets with Jahn-Teller ions, Solid State Comm. **13**, 763 (1973).

[5] D. I. Khomskii and S. V. Streltsov, Orbital effects in solids: Basics, recent progress, and opportunities, Chem. Rev. **121**, 2992 (2021).

[6] M. Enderle, B. Fåk, H.-J. Mikeska, R. K. Kremer, A. Prokofiev, and W. Assmus, Two-Spinon And Four-Spinon Continuum In A Frustrated Ferromagnetic Spin-1/2 Chain, Phys. Rev. Lett. **104**, 237207 (2010); P. Chauhan, F. Mahmood, H. J. Changlani, S. M. Koohpayeh, and N. P. Armitage, Tunable Magnon

Interactions In A Ferromagnetic Spin-1 Chain, *ibid.* **124**, 037203 (2020).

[7] F. Weickert, N. Harrison, B. L. Scott, M. Jaime, A. Leitmäe, I. Heinmaa, R. Stern, O. Janson, H. Berger, H. Rosner, and A. A. Tsirlin, Magnetic anisotropy in the frustrated spin-chain compound $\beta-$TeVO$_4$, Phys. Rev. B **94**, 064403 (2016).

[8] *Quantum Magnetism*, edited by U. Schollwöck, J. Richter, D. J. J. Farnell, and R. F. Bishop (Springer, New York, 2004).

[9] S. Sachdev, Quantum magnetism and criticality, Nat. Phys. **4**, 173 (2008).

[10] F. Sapiña, J. R. guez Carvajal, M. J. Sanchis, R. I. nez, A. Beltrán, and D. Beltrán, Crystal and magnetic structure of Li$_2$CuO$_2$, Solid State Comm. **74**, 779 (1990).

[11] T. Mueller, G. Hautier, A. Jain, and G. Ceder, Evaluation of tavorite-structured cathode materials for lithium-ion batteries using high-throughput computing, Chem. Mater. **23**, 3854 (2011).

[12] M. S. Whittingham, Ultimate limits to intercalation reactions for lithium batteries, Chem. Rev. **114**, 11414 (2014).

[13] S. S. Fedotov, A. S. Samarin, and E. V. Antipov, KTiOPO$_4$-structured electrode materials for metal-ion batteries: A review, J. Power Sources **480**, 228840 (2020).

[14] A. A. Tsirlin, R. Nath, J. Sichelschmidt, Y. Skourski, C. Geibel, and H. Rosner, Frustrated couplings between alternating spin-$\frac{1}{2}$ chains in AgVOAsO$_4$, Phys. Rev. B **83**, 144412 (2011).

[15] F. Weickert, A. A. Aczel, M. B. Stone, V. O. Garlea, C. Dong, Y. Kohama, R. Movshovich, A. Demuer, N. Harrison, M. B. Gamża, A. Steppke, M. Brando, H. Rosner, and A. A. Tsirlin, Field-induced double dome and Bose-Einstein condensation in the crossing quantum spin chain system AgVOAsO$_4$, Phys. Rev. B **100**, 104422 (2019).

[16] U. Arjun, K. M. Ranjith, B. Koo, J. Sichelschmidt, Y. Skourski, M. Baenitz, A. A. Tsirlin, and R. Nath, Singlet ground state in the alternating spin-$\frac{1}{2}$ chain compound NaVOAsO$_4$, Phys. Rev. B **99**, 014421 (2019).

[17] P. K. Mukharjee, K. M. Ranjith, B. Koo, J. Sichelschmidt, M. Baenitz, Y. Skourski, Y. Inagaki, Y. Furukawa, A. A. Tsirlin, and R. Nath, Bose-Einstein condensation of triplons close to the quantum critical point in the quasi-one-dimensional spin-$\frac{1}{2}$ antiferromagnet NaVOPO$_4$, Phys. Rev. B **100**, 144433 (2019).

[18] N. Ahmed, P. Khuntia, K. M. Ranjith, H. Rosner, M. Baenitz, A. A. Tsirlin, and R. Nath, Alternating spin chain compound AgVOAsO$_4$ probed by ^{75}As NMR, Phys. Rev. B **96**, 224423 (2017).

[19] P. K. Mukharjee, K. M. Ranjith, M. Baenitz, Y. Skourski, A. A. Tsirlin, and R. Nath, Two types of alternating spin-$\frac{1}{2}$ chains and their field-induced transitions in $\varepsilon-$LiVOPO$_4$, Phys. Rev. B **101**, 224403 (2020).

[20] M. L. F. Phillips, W. T. A. Harrison, T. E. Gier, G. D. Stucky, G. V. Kulkarni, and J. K. Burdett, Electronic effects of substitution chemistry in the potassium titanyl phosphate (KTiOPO$_4$) structure field: Structure and optical properties of potassium vanadyl phosphate, Inorg. Chem. **29**, 2158 (1990).

[21] L. Benhamada, A. Grandin, M. M. Borel, A. Leclaire, and B. Raveau, KVPO$_5$, an intersecting tunnel structure closely related to the hexagonal tungsten bronze, Acta Cryst. C **47**, 1138 (1991).

[22] K. Momma and F. Izumi, *VESTA* 3 for three-dimensional visualization of crystal, volumetric and morphology data, J. Appl. Crystallogr. **44**, 1272 (2011).

[23] J. Rodríguez-Carvajal, Recent advances in magnetic structure determination by neutron powder diffraction, Phys. B: Condens. Matter **192**, 55 (1993).

[24] A. A. Tsirlin, B. Schmidt, Y. Skourski, R. Nath, C. Geibel, and H. Rosner, Exploring the spin-$\frac{1}{2}$ frustrated square lattice model with high-field magnetization studies, Phys. Rev. B **80**, 132407 (2009).

[25] Y. Skourski, M. D. Kuzmin, K. P. Skokov, A. V. Andreev, and J. Wosnitza, High-field magnetization of Ho$_2$Fe$_{17}$, Phys. Rev. B **83**, 214420 (2011).

[26] R. Nath, D. Khalyavin, K. Somesh, P. K. Mukharjee, and D. T. Adroja, Magnetic structure of frustrated quasi-one-dimensional spin-1/2 chain KVOPO$_4$, STFC ISIS Neutron and Muon Source 10.5286/ISIS.E.RB2000205 (2021).

[27] L. C. Chapon, P. Manuel, P. G. Radaelli, C. Benson, L. Perrott, S. Ansell, N. J. Rhodes, D. Raspino, D. Duxbury, E. Spill, and J. Norris, Wish: The new powder and single crystal magnetic diffractometer on the second target station, Neutron News **22**, 22 (2011).

[28] K. Koepernik and H. Eschrig, Full-potential nonorthogonal local-orbital minimum-basis band-structure scheme, Phys. Rev. B **59**, 1743 (1999).

[29] J. P. Perdew, K. Burke, and M. Ernzerhof, Generalized Gradient Approximation Made Simple, Phys. Rev. Lett. **77**, 3865 (1996).

[30] A. A. Tsirlin and H. Rosner, Ab initio modeling of Bose-Einstein condensation in Pb$_2$V$_3$O$_9$, Phys. Rev. B **83**, 064415 (2011).

[31] H. J. Xiang, E. J. Kan, S.-H. Wei, M.-H. Whangbo, and X. G. Gong, Predicting the spin-lattice order of frustrated systems from first principles, Phys. Rev. B **84**, 224429 (2011).

[32] A. A. Tsirlin, Spin-chain magnetism and uniform Dzyaloshinsky-Moriya anisotropy in BaV$_3$O$_8$, Phys. Rev. B **89**, 014405 (2014).

[33] V. V. Mazurenko, F. Mila, and V. I. Anisimov, Electronic structure and exchange interactions of Na$_2$V$_3$O$_7$, Phys. Rev. B **73**, 014418 (2006).

[34] A. A. Tsirlin, O. Janson, and H. Rosner, Unusual ferromagnetic superexchange in CdVO$_3$: The role of Cd, Phys. Rev. B **84**, 144429 (2011).

[35] S. Todo and K. Kato, Cluster Algorithms For General-S Quantum Spin Systems, Phys. Rev. Lett. **87**, 047203 (2001).

[36] F. Alet, S. Wessel, and M. Troyer, Generalized directed loop method for quantum Monte Carlo simulations, Phys. Rev. E **71**, 036706 (2005).

[37] A. F. Albuquerque, F. Alet, P. Corboz, P. Dayal, A. Feiguin, S. Fuchs, L. Gamper, E. Gull, S. Gürtler, A. Honecker, R. Igarashi, M. Körner, A. Kozhevnikov, A. Läuchli, S. R. Manmana, M. Matsumoto, I. P. McCulloch, F. Michel, R. M. Noack, G. Pawłowski *et al.*, The ALPS project release 1.3: Open-source software for strongly correlated systems, J. Magn. Magn. Mater. **310**, 1187 (2007).

[38] Note that measurements in the weak applied field of 20 mT under zero-field-cooled (ZFC) and field-cooled (FC) conditions showed no bifurcation, thus ruling out spin freezing around or below T_N.

[39] K. Y. Povarov, V. K. Bhartiya, Z. Yan, and A. Zheludev, Thermodynamics of a frustrated quantum magnet on a square lattice, Phys. Rev. B **99**, 024413 (2019).

[40] V. K. Bhartiya, K. Y. Povarov, D. Blosser, S. Bettler, Z. Yan, S. Gvasaliya, S. Raymond, E. Ressouche, K. Beauvois, J. Xu, F. Yokaichiya, and A. Zheludev, Presaturation phase with no dipolar order in a quantum ferro-antiferromagnet, Phys. Rev. Research **1**, 033078 (2019).

[41] M. Skoulatos, F. Rucker, G. J. Nilsen, A. Bertin, E. Pomjakushina, J. Ollivier, A. Schneidewind, R. Georgii, O. Zaharko, L. Keller, C. Rüegg, C. Pfleiderer, B. Schmidt, N. Shannon, A. Kriele, A. Senyshyn, and A. Smerald, Putative spin-nematic phase in BaCdVO$(PO_4)_2$, Phys. Rev. B **100**, 014405 (2019).

[42] N. Shannon, T. Momoi, and P. Sindzingre, Nematic Order In Square Lattice Frustrated Ferromagnets, Phys. Rev. Lett. **96**, 027213 (2006).

[43] R. Nath, A. A. Tsirlin, H. Rosner, and C. Geibel, Magnetic properties of BaCdVO$(PO_4)_2$: A strongly frustrated spin-$\frac{1}{2}$ square lattice close to the quantum critical regime, Phys. Rev. B **78**, 064422 (2008).

[44] R. Nath, V. O. Garlea, A. I. Goldman, and D. C. Johnston, Synthesis, structure, and properties of tetragonal $Sr_2M_3As_2O_2$ ($M_3 = Mn_3$, Mn_2Cu, and $MnZn_2$) compounds containing alternating CuO_2-type and FeAs-type layers, Phys. Rev. B **81**, 224513 (2010).

[45] A. Yogi, A. K. Bera, A. Mohan, R. Kulkarni, S. M. Yusuf, A. Hoser, A. A. Tsirlin, M. Isobe, and A. Thamizhavel, Zigzag spin chains in the spin-5/2 antiferromagnet $Ba_2Mn(PO_4)_2$, Inorg. Chem. Front. **6**, 2736 (2019).

[46] P. Sengupta, C. D. Batista, R. D. McDonald, S. Cox, J. Singleton, L. Huang, T. P. Papageorgiou, O. Ignatchik, T. Herrmannsdörfer, J. L. Manson, J. A. Schlueter, K. A. Funk, and J. Wosnitza, Nonmonotonic field dependence of the Néel temperature in the quasi-two-dimensional magnet $[Cu(HF_2)(pyz)_2]BF_4$, Phys. Rev. B **79**, 060409(R) (2009).

[47] A. A. Tsirlin, R. Nath, A. M. Abakumov, Y. Furukawa, D. C. Johnston, M. Hemmida, H.-A. Krug von Nidda, A. Loidl, C. Geibel, and H. Rosner, Phase separation and frustrated square lattice magnetism of $Na_{1.5}VOPO_4F_{0.5}$, Phys. Rev. B **84**, 014429 (2011).

[48] A. Yogi, N. Ahmed, R. Nath, A. A. Tsirlin, S. Kundu, A. V. Mahajan, J. Sichelschmidt, B. Roy, and Y. Furukawa, Antiferromagnetism of $Zn_2VO(PO_4)_2$ and the dilution with Ti^{4+}, Phys. Rev. B **91**, 024413 (2015).

[49] S. S. Islam, K. M. Ranjith, M. Baenitz, Y. Skourski, A. A. Tsirlin, and R. Nath, Frustration of square cupola in $Sr(TiO)Cu_4(PO_4)_4$, Phys. Rev. B **97**, 174432 (2018).

[50] C. P. Slichter, *Principle of Nuclear Magnetic Resonance*, 3rd ed. (Springer, New York, 1992).

[51] R. Nath, A. V. Mahajan, N. Büttgen, C. Kegler, A. Loidl, and J. Bobroff, Study of one-dimensional nature of $S = 1/2$ (Sr, Ba)$_2$Cu$(PO_4)_2$ and $BaCuP_2O_7$ via ^{31}P NMR, Phys. Rev. B **71**, 174436 (2005).

[52] R. Nath, D. Kasinathan, H. Rosner, M. Baenitz, and C. Geibel, Electronic and magnetic properties of $K_2CuP_2O_7$: A model $S = \frac{1}{2}$ Heisenberg chain system, Phys. Rev. B **77**, 134451 (2008).

[53] T. Moriya, The effect of electron-electron interaction on the nuclear spin relaxation in metals, J. Phys. Soc. Jpn **18**, 516 (1963).

[54] S. Sachdev, NMR relaxation in half-integer antiferromagnetic spin chains, Phys. Rev. B **50**, 13006 (1994).

[55] A. V. Mahajan, R. Sala, E. Lee, F. Borsa, S. Kondo, and D. C. Johnston, ^{7}Li and ^{51}V NMR study of the heavy-fermion compound LiV_2O_4, Phys. Rev. B **57**, 8890 (1998).

[56] The vanadium positions were not refined because of the weak coherent scattering by the V nuclei. These positions were thus fixed to the values reported in Ref. [21]. All the atoms sit at the Wyckoff position 4a. Occupancies of all the atoms were taken to be unity.

[57] D. D. Khalyavin, P. Manuel, M. C. Hatnean, and O. A. Petrenko, Fragile ground state and rigid field-induced structures in the zigzag ladder compound $BaDy_2O_4$, Phys. Rev. B **103**, 134434 (2021).

[58] B. J. Campbell, H. T. Stokes, D. E. Tanner, and D. M. Hatch, *ISODISPLACE*: A web-based tool for exploring structural distortions, J. Appl. Crystallogr. **39**, 607 (2006).

[59] H. T. Stokes, D. M. Hatch, and B. J. Campbell, ISOTROPY *Software Suite*.

[60] A. A. Tsirlin, R. Nath, A. M. Abakumov, R. V. Shpanchenko, C. Geibel, and H. Rosner, Frustrated square lattice with spatial anisotropy: Crystal structure and magnetic properties of PbZnVO$(PO_4)_2$, Phys. Rev. B **81**, 174424 (2010).

[61] R. Nath, A. A. Tsirlin, E. E. Kaul, M. Baenitz, N. Büttgen, C. Geibel, and H. Rosner, Strong frustration due to competing ferromagnetic and antiferromagnetic interactions: Magnetic properties of $M(VO)_2(PO_4)_2$ (M = Ca and Sr), Phys. Rev. B **78**, 024418 (2008).

[62] A. W. Sandvik, Finite-size scaling of the ground-state parameters of the two-dimensional Heisenberg model, Phys. Rev. B **56**, 11678 (1997).

[63] Y. J. Kim and R. J. Birgeneau, Monte Carlo study of the $S = 1/2$ and $S = 1$ Heisenberg antiferromagnet on a spatially anisotropic square lattice, Phys. Rev. B **62**, 6378 (2000).

[64] K. Wierschem and P. Sengupta, Quenching The Haldane Gap In Spin-1 Heisenberg Antiferromagnets, Phys. Rev. Lett. **112**, 247203 (2014).

[65] S. Boudin, A. Guesdon, A. Leclaire, and M.-M. Borel, Review on vanadium phosphates with mono and divalent metallic cations: Syntheses, structural relationships and classification, properties, Int. J. Inorg. Mater. **2**, 561 (2000).